ELECTROCHEMISTRY

Design principles for heterointerfacial alloying kinetics at metallic anodes in rechargeable batteries

Jingxu Zheng[1,2]†, Yue Deng[1]†, Wenzao Li[3,4], Jiefu Yin[5], Patrick J. West[4,6], Tian Tang[1], Xiao Tong[7], David C. Bock[4,8], Shuo Jin[5], Qing Zhao[5], Regina Garcia-Mendez[5], Kenneth J. Takeuchi[3,4,6,8], Esther S. Takeuchi[3,4,6,8], Amy C. Marschilok[3,4,6,8], Lynden A. Archer[1,5]*

How surface chemistry influences reactions occurring thereupon has been a long-standing question of broad scientific and technological interest. Here, we consider the relation between the surface chemistry at interfaces and the reversibility of electrochemical transformations at rechargeable battery electrodes. Using Zn as a model system, we report that a moderate strength of chemical interaction between the deposit and the substrate—neither too weak nor too strong—enables highest reversibility and stability of the plating/stripping redox processes. Focused ion beam and electron microscopy were used to directly probe the morphology, chemistry, and crystallography of heterointerfaces of distinct natures. Analogous to the empirical Sabatier principle for chemical heterogeneous catalysis, our findings arise from competing interfacial processes. Using full batteries with stringent negative electrode–to–positive electrode capacity (N:P) ratios, we show that such knowledge provides a powerful tool for designing key materials in highly reversible battery systems based on Earth-abundant, low-cost metals such as Zn and Na.

INTRODUCTION

Control of chemical reaction kinetics at a heterointerface is required in multiple chemical transformations, including ammonia synthesis (*1*), hydrocarbon reforming (*2*), and water-gas shift reactions (*3*) to achieve economic viability at commercial scale. All of these processes typically involve multiple and complex physiochemical kinetic steps occurring on the surface of a solid with specific catalytic activity for one or more reactants; they are here collectively termed heterocatalysis. Driven by the fundamental challenge of rationally designing substrates with high and selective activity to speed up conversion of inexpensive reactants into high-value products and commercial interest in performing these reactions on a large scale, research centering on heterointerfacial chemical reactions has flourished for at least the past 100 years (*4*, *5*). Here, we consider a successful empirical design concept, the Sabatier principle—which has provided a useful framework for organizing heterocatalysis data—in what might at first appear an unrelated context, electrical energy storage in batteries using metallic anodes. The Sabatier principle states simply that the highest chemical activity is achieved when the interaction between reactant molecules and the catalyst surface is at an optimal value (*6*, *7*), i.e., neither too weak nor too strong.

Figure 1 is the starting point of our analysis. It illustrates the similarities between the physicochemical sequence that leads to growth/dissolution of a metal electrode in a rechargeable battery and those that govern reversible chemical transformations on the surface of catalyst particles, e.g., hydrogen evolution reaction and hydrogen oxidation reaction on Pt (*8*). Considering that unlike the latter scenario, the reactant undergoes a coupled redox reaction and phase change in the former, we wondered whether an analogous Sabatier-like design principle exists and whether the principle could be used for electrode design/selection in rechargeable metal batteries to achieve high reversibility. The answer to this question is particularly critical to metal anodes with low negative electrode–to–positive electrode capacity (N:P) ratios or those utilizing a so-called "anode-free" configuration. In these cases, reversible metal plating/stripping on a heterosubstrate, as opposed to the metal itself, is inevitable during battery cycling.

As the first step to evaluate this conjecture, we investigated zinc metal plating/stripping in aqueous electrolytes. Our motivation for studying aqueous zinc batteries is straightforward. First, secondary/rechargeable batteries based on Earth-abundant and low-cost metals such as Zn, Na, and Al are among the most promising solutions for high–energy density, low-cost, and long-term storage of electric power at scales compatible with the rapidly rising scale of global production of electricity from renewable wind and solar photovoltaic resources (*9*, *10*) and which can handle both the diurnal and seasonal variability in energy supply from these sources (*11*, *12*). Second, Zn metal has a moderate redox potential, which means that electrochemical processes at a Zn electrode can be more easily decoupled from chemical and electrochemical parasitic reactions with electrolyte components, which are known to lower the reversibility of metals such as Li and Na (*10*), allowing us to focus on the chemical kinetics between the metal and the substrate at the heterointerface. Last, analogous to conventional heterocatalytic processes (*13*), the electrochemical and physical transformations that control the charge (electroreduction) and discharge (ion dissolution/solvation) processes at the solid-liquid heterointerface in a Zn battery electrode place quite different and even competing demands for the electrode and electrolyte design.

[1]Department of Materials Science and Engineering, Cornell University, Ithaca, NY 14853, USA. [2]Department of Physics, Massachusetts Institute of Technology, Cambridge, MA 02139, USA. [3]Department of Chemistry, State University of New York at Stony Brook, Stony Brook, NY 11794, USA. [4]Institute for Electrochemically Stored Energy, Stony Brook University, Stony Brook, NY 11794, USA. [5]Robert Frederick Smith School of Chemical and Biomolecular Engineering, Cornell University, Ithaca, NY 14853, USA. [6]Department of Materials Science and Chemical Engineering, State University of New York at Stony Brook, Stony Brook, NY 11794, USA. [7]Center for Functional Nanomaterials, Brookhaven National Laboratory, Upton, NY 11973, USA. [8]Interdisciplinary Science Department, Brookhaven National Laboratory, Upton, NY 11973, USA.
*Corresponding author. Email: laa25@cornell.edu
†These authors contributed equally to this work.

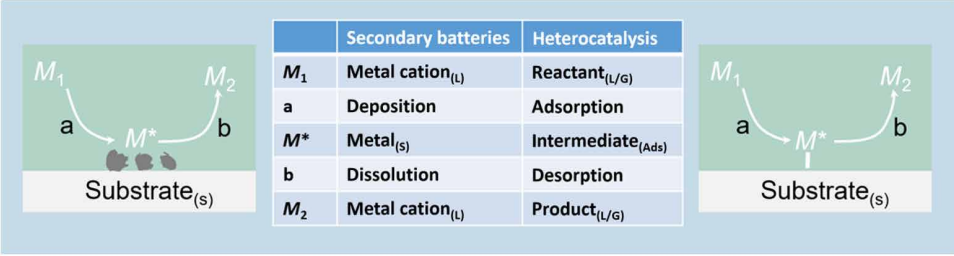

Fig. 1. Chemical reaction path at a heterointerface. Reactions in metallic anodes of secondary batteries (left) and in heterogeneous catalysis (right). In both scenarios, the reactant species first "attaches" to and then "detaches" from the surface of a solid, as labeled by "a" and "b," respectively.

It is also known that for rechargeable batteries of any chemistry to offer cost-competitive storage of electric power, high levels of electrode reversibility are required to enable long operating lifetimes and, consequently, low amortized system costs. Understanding and controlling the chemical kinetics of reversible deposition/dissolution of metals at heterointerfaces in battery electrodes are therefore fundamental requirements for progress. On the one hand, it is understood that the irreversibility of plating/stripping processes at a metal battery anode is the dominant source of degradation of storage capacity with time (*9*) and is also associated with serious safety risks associated with internal shorting (*14*). On the other hand, multiple physiochemical processes are actively involved, such as crystal nucleation and growth (*15*), diffusion, and convection, and therefore, control is challenging (*16*, *17*). A diversity of strategies has been proposed to address these challenges, including electrolyte design (*18*, *19*), electrode architecture design (*20*, *21*), and surface chemistry/interphase design (*12*, *22*). Redox chemistry at heterointerfaces has also been leveraged in some studies, via intentional, a priori chemical design of the substrate or through ion exchange chemistry of electrolyte additives to regulate growth of the electrodeposited metals. Strong chemical binding/interactions between the substrate and the metal deposited at the heterointerface, also known as the "metallophilicity," are conventionally thought to improve control of deposit morphology in either case by enabling a uniform nucleation landscape for electrodeposit growth (*23*, *24*).

A first requirement for our studies is to create a series of heterointerfaces that are of high quality, that exhibit good uniformity, and that enable the interaction strengths with Zn metal to be tuned. A common approach for manipulating binding strength is to dope carbonaceous materials with heteroatoms (*22*). The approach is unattractive here because it introduces complications (e.g., the typically used carbon-based materials are associated with nontrivial geometries, e.g., anisotropic shape and high specific surface area) (*25*), which could play additional unexpected roles in electrodeposition (e.g., by altering the local electric field distribution at the substrate) (*12*), confounding any serious efforts at deconvoluting and evaluating the contribution from interfacial chemical kinetics.

Here, we instead leverage Zn's known capability to form alloys with other metals upon electroreduction as reported in early literature (*26*, *27*). These metals are commercially available as foils, which offer a well-defined, planar geometry as is evident from scanning electron microscopy (SEM) topographic and atomic force microscopy (AFM) roughness analysis (fig. S1). Given the rich chemistries achievable on metals that have different interaction strengths with Zn, it is possible to semiquantitatively evaluate the role played by heterointerfacial chemical kinetics in electroplating/stripping.

RESULTS

We first used cyclic voltammetry (CV) as a classical electroanalytical tool (*28*) to interrogate the electrochemical reactions occurring at a representative set of metal substrates in a range of chemistries: stainless steel (SS), aluminum (Al), tantalum (Ta), copper (Cu), silver (Ag), and gold (Au). In the CV experiments, the metal substrate is used as the working electrode in an electrochemical cell and is immersed in a conventional Zn battery electrolyte, 2 M $ZnSO_4$ (aq). The results reported in Fig. 2 show the current-potential (*i*-*V*) responses. The differences are stark, large, and systematic. On SS, Al, and Ta, only the metal plating and stripping peaks are detectable. For example, in a negative scan, the response currents above 0 V versus Zn^{2+}/Zn are negligible, i.e., <0.5 mA/cm^2 (Fig. 2, A and B), and the standard $Zn^{2+} \rightarrow Zn_{(s)}$ reaction is detected as the potential enters the regime below 0 V versus Zn^{2+}/Zn. In contrast, response currents of two orders of magnitude higher are observed above 0 V versus Zn^{2+}/Zn on Cu (Fig. 2, C to E), Ag (Fig. 2, F to H), and Au (Fig. 2, I to K), respectively, in addition to the Zn plating current below 0 V versus Zn^{2+}/Zn.

Clues about the origins of the *i*-*V* responses can be found in prior studies. Specifically, the "underpotential deposition" behaviors of Zn on Cu, Ag, and Au are attributable to spontaneous alloying between the metal substrate and metal deposits (*29*). The Zn alloys exhibit a lower free energy than elemental Zn, resulting in a smaller potential required to reduce Zn^{2+} (*30*). Further quantitative examination of the *i*-*V* responses of Cu, Ag, and Au reveals subtle but critical differences in alloying mechanism. We plot the peak current i_p over a series of scan rates v in Fig. 2 (E, H, and K). Ag and Au show a characteristic $i_p \sim v^{1/2}$ scaling behavior, while Cu manifests a linear relation $i_p \sim v^1$. The R^2 values of the fittings are 0.99, 0.96, and 0.998 for Ag, Au, and Cu, respectively. We conclude that whereas Ag and Au undergo diffusion-controlled, bulk conversion–type alloying processes as described by the Randles-Sevcik equation, alloying between Cu and Zn progresses by a "pseudo-capacitive"–like route (*31*). This suggests that the Cu-Zn alloying reaction is confined to a thin skin layer on the substrate, which is consistent with the pseudo-capacitive $i_p \sim v$ scaling relation apparent from the CV experiments.

Conclusions from our indirect electroanalytical analyses of the reaction currents are corroborated by findings from more in-depth characterization of the electrodeposited phases. X-ray diffraction (XRD) is used to directly capture the crystallographic transitions occurring on the substrates (Fig. 3). The results show that SS, Al, and Ta remain chemically intact after Zn plating, not undergoing any detectable reaction with Zn metal. In contrast, diffraction patterns assigned to intermetallic compounds, i.e., ε-$CuZn_4$, ε-$AgZn_3$, and $AuZn_3$ + AuZn,

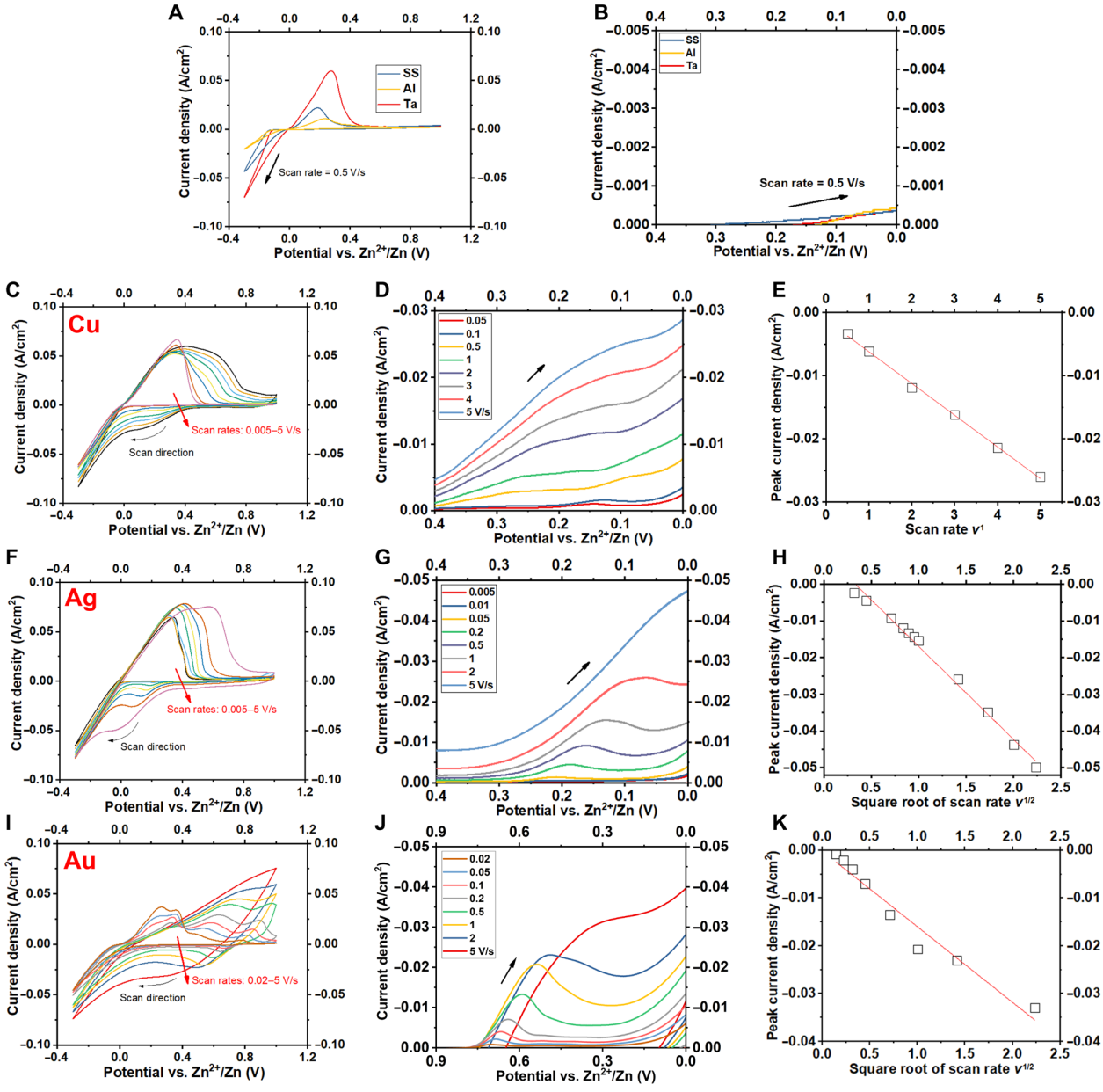

Fig. 2. CV of Zn metal plating/stripping on substrates of different chemistries. CV scans in the range -0.3 to +1.0 V versus Zn^{2+}/Zn at various metal electrodes substrates in a conventional 2 M ZnSO4 (aq) electrolyte: (**A**) stainless steel, Al and Ta, respectively; (**B**) the enlarged plot showing the underpotential regime in the cathodic scans. (**C**) CV scans, (**D**) enlarged plot of CV and (**E**) plot of peak current density versus scan rate (i_p versus v in V/s) for Cu. (**F**) CV scans, (**G**) enlarged plot of CV and (**H**) plot of peak current density versus square root of scan rate (i_p versus $v^{1/2}$, in $V^{1/2}/s^{1/2}$) for Ag. (**I**) CV scans, (**J**) enlarged plot of CV and (**K**) plot of peak current density versus square root of scan rate (ipversus $v^{1/2}$, in $V^{1/2}/s^{1/2}$) for Au.

are detected on Cu, Ag, Au, respectively. The stronger alloy peaks (labeled by the cross +) observed for Ag and Au, relative to those seen for the Cu substrates, imply that the amounts of alloy formed on the former two are substantially greater than the latter after cycling. This observation is consistent with the argument that Ag and Au undergo bulk conversion with Zn, but the reaction on Cu is limited to a thin layer.

Figure 4 reports the electrochemical galvanostatic plating/stripping behaviors of Zn on the same metal foil substrates. As can be seen in Fig. 4A, the substrate chemistry has a strong influence on the plating/stripping cycling reversibility of Zn as quantified by the Coulombic efficiency (CE) = $\frac{\text{stripping capacity}}{\text{plating capacity}} \times 100\%$ (see also Materials and Methods and fig. S2 for additional information). We note further that the current density used is well below the diffusion limit (*32*). These results therefore lead to two conclusions: (i) SS, Al, and Ta are less effective substrates for achieving high Zn reversibility because they lead to a broader distribution of CE values than Cu, Ag, and Au, indicating unstable plating/stripping process, and (ii) Cu, Ag, and Au all show relatively narrow CE distributions, but Au has a lower CE value corresponding to low plating/stripping reversibility.

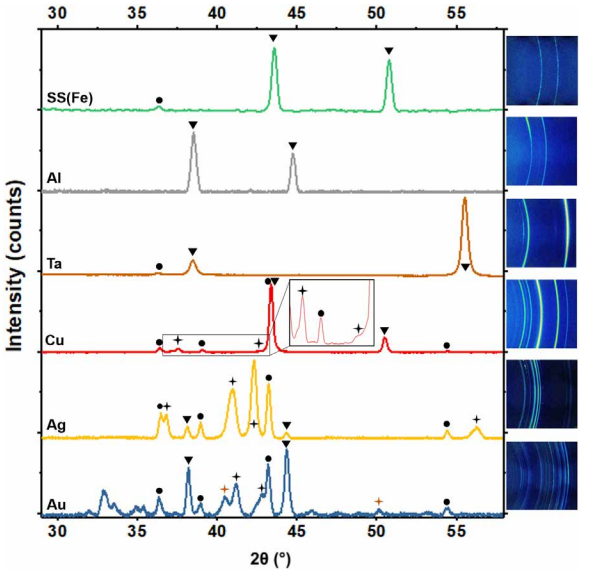

Fig. 3. XRD analysis of various metal substrates after Zn plating/stripping cycling. ●, Zn metal; ▼, substrates; ┼, intermetallic phases. The respective two-dimensional XRD patterns are provided on the right. Sample condition: after 100 cycles at 8 mA/cm^2, 0.8 mAh/cm^2, with Zn deposition (0.8 mAh/cm^2) remaining on the substrate before cell dissembling. Zn deposits could be peeled off and stuck in the porous glass fiber separators if the interface between Zn and the substrates is not mechanically robust. Hence, the Zn deposits may not appear in the XRD patterns.

The diverse plating/stripping behaviors on different metal substrates can be understood by examining the voltage profiles of the plating/stripping cycles as shown in Fig. 4 (B to H). For SS, Al, and Ta where broad CE distributions are seen, the stripping process consistently features spiky, erratic voltage evolution; in stark contrast, the voltage profiles of Zn stripping on Cu, Ag, and Au are smooth and stable (see also fig. S3 for Zn plating/stripping on Cu with a lower cutoff voltage). The voltage profiles of SS, Al, and Ta are indeed suggestive of an undesirable process termed metal orphaning (*33*–*35*). The behavior of Ti foil, another conventional substrate used for evaluating Zn plating/stripping, is similar to SS, Al, and Ta (fig. S4). See also figs. S5 and S6 for measurements made at other capacities. In the orphaning process, the metallic, solid electrodeposits are physically disconnected from the electron source at the electrode, thereby becoming electrochemically inactive/dead. The sudden potential drops and the sometimes >100% CE values are caused by random reconnection of inactive/dead metal fragments over cycling (*32*, *35*). Both the nonuniformity of the deposition and ease of physical detachment from the substrate are related to the propensity of the electrodeposited metal to orphan.

To experimentally verify this interpretation, we use optical microscopy and SEM to characterize the separator membrane facing the heterointerface after plating/stripping cycling (figs. S7 and S8). The results show that large amounts of Zn metal electrodeposits on SS, Al, and Ta become electrochemically inactive and are stuck in the separator during repeated plating/stripping, while no dead Zn is observable on Cu and Ag substrates. On the separator facing an Au substrate, coarse, dark brownish powders are observed under the optical microscope, which are identified as an intermetallic phase (AuZn; brown cross ┼) by XRD (fig. S9), as opposed to dead metallic Zn.

We further examined the galvanostatic plating/stripping voltage profiles to assess the resistances to electrochemical change. The first observation is that a prominent nucleation overpotential exists at the onset of Zn plating on SS, Ta, and Al but not on Cu, Ag, and Au; instead, pronounced capacities above 0 V versus Zn^{2+}/Zn are detected that are attributable to the alloying reactions. Spontaneous alloying processes can also occur after the electrodeposition, directly between Zn metal and the substrate. This portion of alloying reaction is not captured by the capacity above 0 V versus Zn^{2+}/Zn in the plating branches of the galvanostatic voltage profiles. The presence of a secondary plateau in the stripping voltage profile is also noticeable. The secondary plateau corresponds to the dealloying process, which occurs after the stripping of elemental zinc. These identified signatures of the interfacial reaction are in good agreement with the CV results (Fig. 2) and the XRD results (Fig. 3 and fig. S10); see also x-ray photoelectron spectroscopy (XPS) in fig. S11. Focused ion beam (FIB) and advanced aberration-corrected atomic-resolution scanning transmission electron microscopy (STEM) were used to further characterize these alloying phenomena (Fig. 5, A to C, and figs. S12 to S15). In addition, as shown in figs. S16 to S18, we performed Zn plating/stripping efficiency measurement on a nonplanar SS mesh to evaluate the possible influence from substrate roughness. The result shows that roughness on these scales have, at most, a negligible influence on Zn plating/stripping, in comparison with the interfacial chemistry.

DISCUSSION

Together, our findings indicate that chemical interaction at the heterointerface is necessary to effectively prevent detachment of metal deposits, in analogy to the first component to the Sabatier principle. That is, moderate chemical interaction is needed to promote adsorption of the molecules to the catalyst surface. We believe that the alloying-induced adhesion is comparable to the concept of "diffusion welding" in metallurgy (*36*, *37*). Such diffusion welding is thermodynamically driven by alloying reactions, i.e., the formation of metal-metal solid solution and/or intermetallics. Unlike a conventional thermal- or pressure-driven diffusion welding process, diffusion in this scenario is mainly driven by a spontaneous chemical reaction. This is allowed due, in part, to the relatively low melting temperature of Zn (T_m = 698 K). At room temperature, Zn has a moderate homologous temperature $T_H = \frac{T}{T_m} = 0.4$, suggesting that interdiffusion of Zn can occur on moderate time scales (*38*). Motivated by this analysis, we summarize the melting temperatures and the T_H values of metals of contemporary interest as battery anodes (see table S1). Our findings imply that the diffusion welding mechanism is likely to play an even more important role for the alkali metal electrodes and possibly some role for Al electrodes.

One may naïvely conclude that a stronger alloying interaction would provide a greater driving force for the interdiffusion and further suppress the detachment of metal deposits. We interrogated the reversibility of Zn electrodeposition on three metal substrates, Cu, Ag, and Au, which all show some chemical interaction with Zn, but quite different electrochemical characteristics. The capacity contributed by the secondary plateau in the stripping process is used as a parameter for comparison across Cu, Ag, and Au: capacities are 0.08, 0.23, and 0.49 mAh/cm^2 (accounting for 10, 25, and 70% of the total stripping capacity) and are attributed to dealloying reaction of

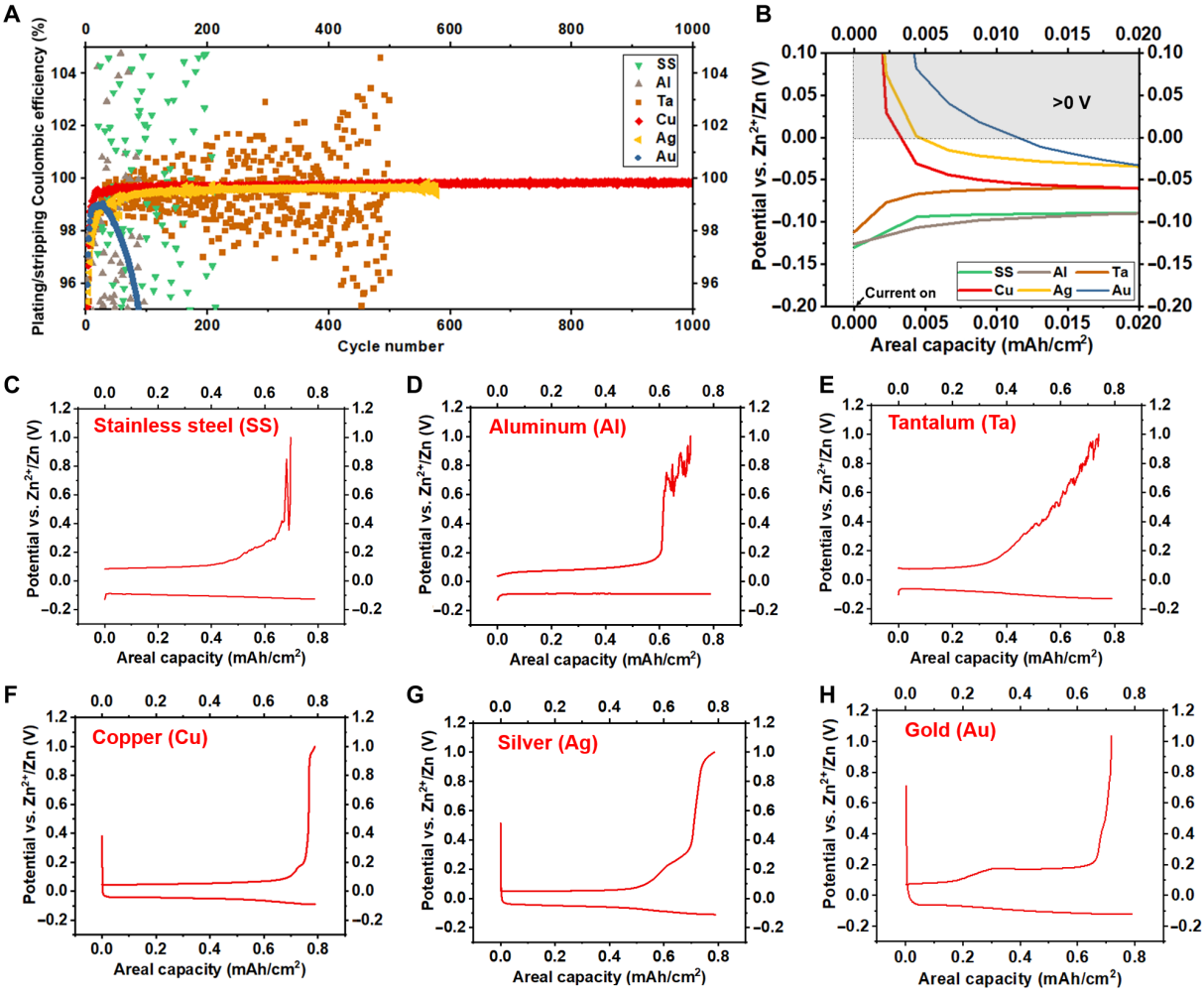

Fig. 4. Galvanostatic electrochemical deposition/dissolution behaviors of Zn on substrates of different chemistry. (**A**) Coulombic efficiency (CE) for Zn plating/stripping as a function of cycle number. (**B**) Voltage evolution in the nucleation regime. Representative plating/stripping voltage profiles of Zn plating/stripping on (**C**) SS, (**D**) Al, (**E**) Ta, (**F**) Cu, (**G**) Ag, and (**H**) Au. The spiky nature of the stripping voltage profiles observed on SS, Al, and Ta is consistent with expectations for formation of "orphaned" Zn metal. Secondary voltage plateaus are observed on Cu, Ag, and Au. Current density, 8 mA/cm^2.

Zn from Cu, Ag, and Au, respectively. The amount of this secondary capacity is negatively correlated to the reversibility (i.e., CE) and the cycle life achieved on the three substrates. This explicitly contradicts the conventional wisdom of a monotonic dependence of metal plating/stripping performance on the strength of the heterointerfacial chemical affinity. More insights can be obtained by comparing the galvanostatic plating/stripping efficiencies to the results obtained from the CV and XRD experiments discussed earlier. The greater dealloying capacities of Ag and Au substrates are indicative of the bulk conversion, while the interaction between Zn and Cu is limited to the surface.

This last inference is supported by SEM characterization of the surface topology of the cycled substrates (fig. S19)—Cu remains almost intact, while Ag and Au develop into porous structures. We note that this finding is consistent with the observation of a considerable amount of pulverized AuZn intermetallic phase stuck in the separator (figs. S7 to S9). It means that a strong chemical interaction will result in bulk phase transition, which pulverizes the substrate, causes incomplete dissolution of the deposited metal [e.g., see Fig. 5 (A to C); incomplete Zn dissolution only found on Ag but not on Cu after cycling], and ultimately leads to battery failure. The extreme cases are demonstrated by Si, Sn, Ag, and so forth when they are paired with Li metal (*39*–*41*). A large initial irreversibility and quick capacity fading is consistently observed. The optimal case in the Zn system is exemplified by Cu, where the substrate offers what appears to be a just right, moderate degree of interaction at the heterointerface with the metal deposits—neither too weak, which causes detachment of dead metal, nor too strong, which induces phase transitions penetrating the bulk. The pseudo-capacitive behavior in the underpotential regime (i.e., >0 V versus Zn) of a negatively polarized voltage sweep provides an easily accessible signature of substrates where such limited, interfacial chemical interaction exists and presages high levels of reversibility in metal anodes of batteries. These analyses could be used to interpret the observed variation of reversible plating/stripping behaviors over substrate chemistry (Fig. 5D and fig. S20). We performed additional electrochemical measurements to evaluate the possible influences of surface oxide layer, desolvation structure, and electrolyte decomposition on plating/stripping

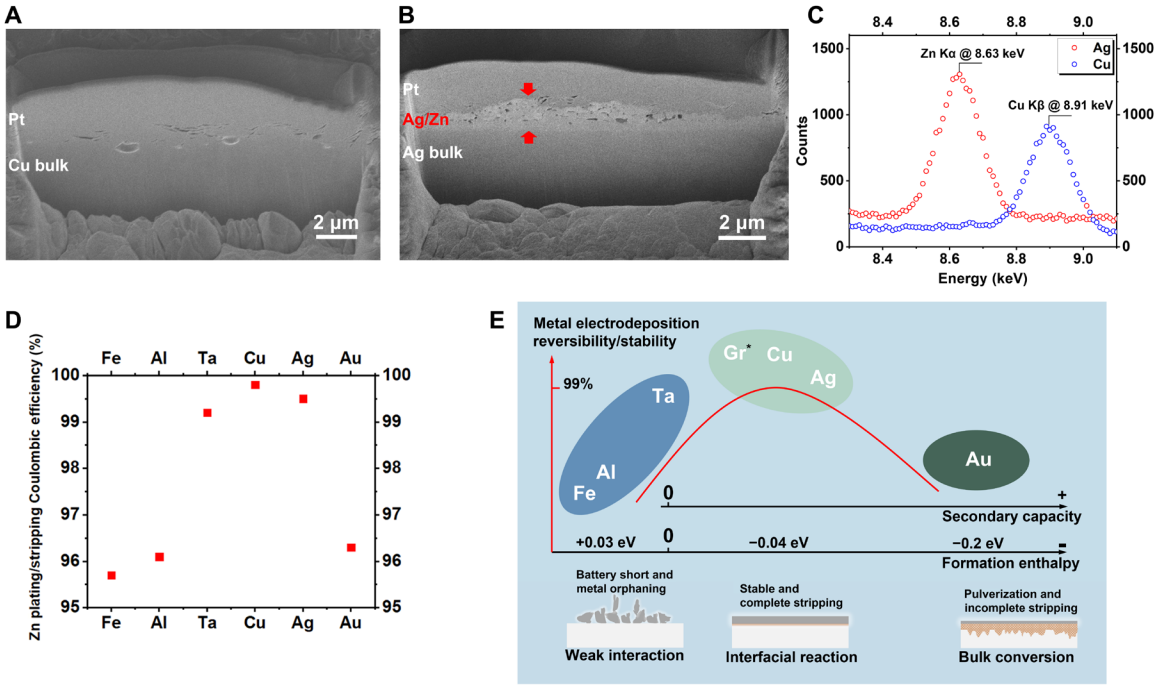

Fig. 5. A Sabatier-like principle for reversible metal deposition/dissolution at battery anodes. FIB-SEM characterization of (**A**) Cu and (**B**) Ag electrodes after Zn plating/stripping. A Pt protection layer is deposited on electrode surface before FIB. (**C**) Energy-dispersive spectroscopy near the Zn Kα energy (i.e., 8.63 keV) collected at the two interfaces formed on Ag and Cu. See more details in figs. S12 to S15. (**D**) The average values and the SDs of the metal plating/stripping CE of the substrates. (**E**) The proposed qualitative volcano-shaped relation in battery anodes. Gr*, graphene.

behaviors; the results suggest that they do not act as the determinant factor in scenarios studied in this work (figs. S21 to S23).

In the original Sabatier principle for heterogeneous catalysis, enthalpy of formation of the adsorbed species is used as a representative parameter for qualitatively evaluating the interaction strength. A more negative enthalpy means that more heat is released by the reaction and therefore indicative of stronger interactions. Here, an obvious, phenomenological relation can be seen—the dependence of plating/stripping reversibility on the capacity contributed by the secondary reaction (Fig. 5E); both the cases of no secondary reaction and excessive secondary reaction are unfavorable. We note that use of secondary capacity as a phenomenological parameter is also advantageous as it reflects the fundamental thermodynamic and kinetic parameters intrinsic to the chemistry.

Reorganizing the results using this scheme, we observe a similar volcano-like qualitative trend of electrochemical plating/stripping reversibility/stability over the range of formation enthalpy of the intermetallic species explored (Fig. 5E) (*12*, *23*, *42*, *43*). Ta is a widely known refractory, inert metal, which has been used to make crucibles to contain Zn for identifying the binary phase diagrams of Zn (e.g., U-Zn and Mn-Zn). We therefore assumed that the interaction between Ta and Zn are thermodynamically unfavorable at room temperature, suggesting a positive formation enthalpy of Ta-Zn intermetallics. Judging from the electrochemical performance in Fig. 4 and the visualization results in figs. S7 and S8, the interaction between Ta and Zn is weaker than Cu-Zn, but stronger than SS-Zn and Al-Zn. As semiquantitatively shown in the plot, SS (Fe and Cr), Al, and Ta have positive formation enthalpies with Zn; Cu, Ag, and Au have negative formation enthalpies with Zn, but the value for Au is approximately four to five times greater than Cu and Ag. The greater heat dissipation generated by Au than by Cu and Ag upon Zn deposition is experimentally confirmed by in operando microcalorimetry (fig. S24) (*44*). This analysis is in excellent agreement with the observed plating/stripping performance—Cu and Ag show much higher reversibility and stability than the metals on the left side (e.g., SS, Ta, and Al) and the metals on the right side (e.g., Au). The electronegativity χ of these elements follows a sequence of Ta(1.5) < Ti(1.54) < Al(1.61) < Zn(1.65) < Cr(1.66) < Fe(1.83) < Cu(1.90) < Ag(1.93) < Au(2.54); this trend indicates that a greater $\Delta\chi = \chi_M - \chi_{Zn}$ may induce a stronger charge transfer effect between Zn and the substrate metal M and thus a stronger chemical bonding. We note further that, in some other cases, the alloying reaction between the metal deposits and the substrate could, be suppressed by surface passivation (e.g., the presence of an oxide layer). This results in a scenario that falls onto the weak-interaction side. Viewed in a broader context, this framework can alternatively be used to comprehend other physical interactions between the metal deposit and the substrate. Earlier studies report that Zn exhibit extremely stable, reversible plating/stripping on graphene substrate (*12*). The adsorption energy of Zn onto graphene is −0.02 eV (*23*), very close to the optimal values identified in the present work.

The ease of tuning the reaction rate of the plating/stripping reaction by varying the externally imposed current offers an additional dimension for understanding heterointerfacial electrochemical phenomena in batteries. The ratio of the deposition rate and the alloy-forming reaction rate is a natural dimensionless group to capture the influence of the current density. On the basis of the results in the preceding sections, one would expect that the negative effects of excessive alloying reactions observed on Ag and Au on electrode reversibility should be exacerbated at lower deposition rates but

attenuated at higher rates. As shown in fig. S25, the observations from experimental plating/stripping measurements are highly consistent with this expectation. At a low current density (i.e., 2 mA/cm^2), Ag and Au exhibit more pronounced alloy formation behaviors, as evidenced in the potential profile. This is accompanied by a clear deterioration in electrode reversibility as the current density decreases. At a high current density of 40 mA/cm^2, the traits of excessive alloying reactions are hardly observable, and the CE values of the substrates are notably improved. An additional notable finding is that the plating/stripping remains highly stable on Cu at all current densities and areal capacities (see also figs. S26 and S27). This suggests the interfacial nature of this process, underscoring the importance of our earlier observation that a moderately strong chemical interaction at the interface represents the optimal case for reversible plating/stripping of metals in battery anodes.

It is important to point out here that while the considerations based on energy (i.e., formation enthalpy) appear to be fairly effective in qualitatively predicting the observed trends, the kinetic aspects, e.g., the solid-state transport and the intrinsic chemical reaction rate, can play nontrivial roles. For example, the diffusivity of Zn in Ag is generally reported to be higher than that in Cu (*45*–*47*). This could originate from the larger atomic radius of Ag (Zn, 142 pm; Cu, 145 pm; and Ag, 165 pm). The larger Ag lattice may allow additional diffusion mechanisms. Notwithstanding the kinetical aspects, a reasonably good design rule can still be deduced from the data from an energy standpoint, namely, that a very negative formation enthalpy is consistent with a strong propensity of the system for undergoing bulk transition and invariably causes volume change that, after many plating/striping cycles, causes fatigue failure and pulverization of the substrate (*48*). This may, in turn, accelerate the transport kinetics. We further point out that the tendency for Zn to form solid-solution phases with Cu, Ag, and Au could be an important kinetic step in the formation of intermetallic phases where the parent lattices of the substrates are initially preserved, in the solid-solution formation step, but later on transformed, in the intermetallic formation step. The absence of solid solutions in the phase diagram may result in sluggish kinetics that prevent these heterointerfacial alloying reactions from occurring at time scales relevant to general battery operation (i.e., minutes to hours) at room temperature. The energy scale associated with solid-solution formation, for example, between Zn and Cu, is on the order of −0.01 eV (*49*, *50*); this means that alloying reactions of such a nature could also be sufficient to promote diffusion welding. A complete prediction may require detailed ab initio simulation to capture the kinetics step by step and the remaining aspects of the intermetallic phase formation, e.g., volume change and elasticity. The next step toward an atomistic, computational understanding of the system could be based on experimental measurements performed on single-crystalline substrates.

We note further that achieving highly stable and reversible Zn plating/stripping and leveraging it to advance the development of rechargeable batteries are of immediate interest to the growing community interested in low-cost, Earth-abundant electrochemical couples capable of storing large amounts of electrical energy. A close to unity plating/stripping reversibility is required, for example, to create commercially relevant Zn battery systems (fig. S28), because it minimizes the amount of Zn needed in the battery anode and lowers the amortized battery costs (*51*). As suggested by the plating/stripping CE results shown in Fig. 4, Cu stands out as a promising substrate for Zn anodes (see also fig. S29 for CE measured at 40 mA/cm^2: 99.94% over 10,000 cycles). Motivated by these observations, we assembled Zn full-cell batteries by paring the Zn anode of interest with an imperfect but state-of-the-art vanadium-based cathode (see fig. S30 for more details of the cathode design) (*52*). As a proof-of-concept demonstration, we deposit a known amount of Zn metal onto Cu and SS and harvest them as two representative Zn anodes for full-battery evaluation. We intentionally use a somewhat stringent N:P ratio of 3:1, which is approximately more than two orders of magnitude lower than conventional N:P values for Zn battery studies based on commercial Zn foil. Reversible metal plating/stripping on heterosubstrates is inevitable in these scenarios, i.e., with low N:P ratios or even anode-free. The battery performance reported in Fig. 6 shows that the Zn on Cu anode manifests stable cycling over 500 cycles with a 73% capacity retention (91% after 100 cycles), which outperforms the Zn on SS anode (see also fig. S31). It should be noted that the cathode material makes the dominant contribution to the observed capacity decay. More impressive is that the Zn on Cu electrode with an N:P ratio of 3:1 is no worse than commercial Zn foil with an N:P > 100:1. This observation means that via manipulating the chemical kinetics at the heterointerface, only <5% of the originally needed Zn is required here to achieve a same level of battery performance.

Because of the interfacial nature of the Sabatier-type principle, a thin coating of a rationally chosen substrate should be sufficient. Results in figs. S32 to S37 show that by coating a thin Cu skin layer (0.36 mg/cm^2) onto the SS substrate, the propensity of Zn for forming dead fragments observed on SS is completely suppressed. This means that, essentially, any substrate (probably chosen for other

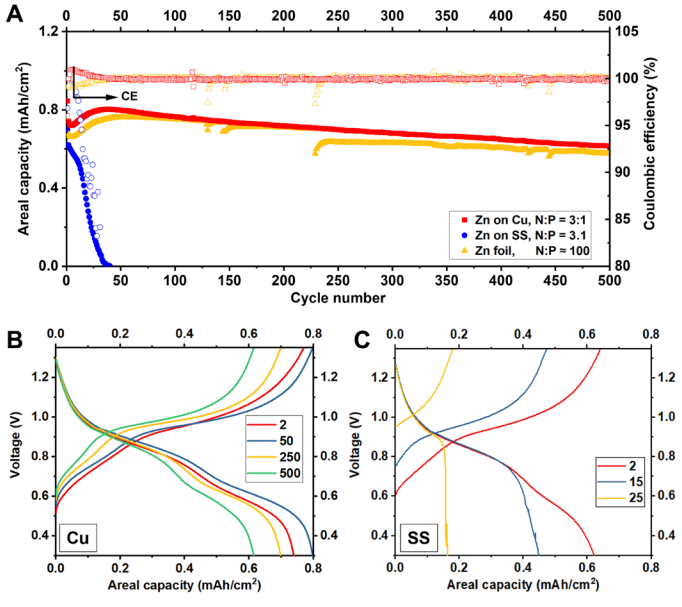

Fig. 6. Full-battery cell demonstration under stringent active material loading conditions. (**A**) Cycling performance of Zn||NaV_3O_8 full cells. A certain amount of Zn metal is deposited on Cu or SS and used as the anode. The performance of commercial thick Zn foil is also tested. The areal capacity is ~0.7 mAh/cm^2, the current density is 1.3 mA/cm^2, and the cathode area is ~1 cm^2; the N:P ratio is maintained at 3:1 for Zn on Cu and Zn on SS. Charge-discharge voltage profiles of batteries using Zn deposited on (**B**) Cu and (**C**) SS. The numbers in the legends of (B) and (C) denote the cycle numbers. Solid data points and open data points represent the capacity (left *y* axis) and the CE (right *y* axis), respectively.

reasons, e.g., lightweight) can be tailored using standard deposition methods to achieve favorable surface chemistry for the purpose of promoting highly reversible metal plating/stripping in battery anodes.

Last, in light of the universality of the fundamental processes that underlie our concept, we wanted to explore the relevance of the "Sabatier"-like principle to metal electrode reversibility in an entirely different context, i.e., charge and discharge of sodium (Na) metal anodes. Na is, like Li, a body-centered cubic metal, is highly reactive, and has a much lower reduction potential than Zn. Na is also mechanically fragile at room temperature and prone to orphaning (*52*) and is conventionally assumed to require formation of a stable solid-electrolyte interphase (SEI) for reversible plating/stripping at planar substrates. We choose Au as a model substrate for Na deposition and in-depth analysis. Na-Au is attractive for fundamental and application-related reasons. From a more fundamental perspective, density functional theory calculations report that its formation enthalpy per atom is −0.283 eV, which is comparable to the formation enthalpy of Zn-Au. This strong interaction reflects the large $\Delta\chi = 2.54 - 0.93 = 1.61$ between Na and Au. The large gap in electronegativity suggests a strong charge transfer effect between Na and Au when alloyed. From an applications perspective, Na is among the most promising candidates for electrical energy storage in the mass-manufactured, low-cost batteries needed to enable an "electrify everything" future.

Despite the obvious differences between Zn and Na, the Sabatier-like principle appears relevant for designing substrates for achieving highly reversible Na metal deposition. Comparing Zn-Au and Na-Au, it is apparent and expected that the XRD and electrochemical responses of Au-to-Na plating/stripping (Fig. 7, A to D) show that Na-Au falls into the category of "too-strong" interaction, i.e., the right side of the Sabatier-like relation (Fig. 5). The Sabatier-like framework offers a straightforward approach for securing highly reversible deposition of Na on Au: maintain the thickness of the Au layer below a certain value where the substrate bonding contribution is just right to prevent metal orphaning but still weak enough to enable complete recovery during the stripping process. In other words, the thickness of the Au substrate can serve as a highly effective knob for tuning the metal-substrate interaction and therefore Na plating/stripping reversibility. The results reported in Fig. 7D show that thinning down of the Au coatings to values in the range of 10 to 100 nm drives the interaction into a more interfacial, stable regime, as evidenced by Na plating/stripping voltage profiles. These profiles are evidently similar to those reported earlier for Zn-Cu (Fig. 4F). Figure 7 (E and F) shows further that these changes also result in high Na plating/stripping reversibility, with an optimal CE value of >99% achieved on the Au film with a thickness of 50 nm. A more detailed discussion of these findings is provided in note S1.

In summary, we report a simple, yet powerful design principle for achieving reversible metal electroplating/stripping behaviors at a heterointerface. Analogous to the Sabatier principle for heterogeneous chemical catalysis, we specifically find that a moderate interfacial chemical interaction strength between the metal and the substrate is favorable. This discovery is also in line with the recent progress of

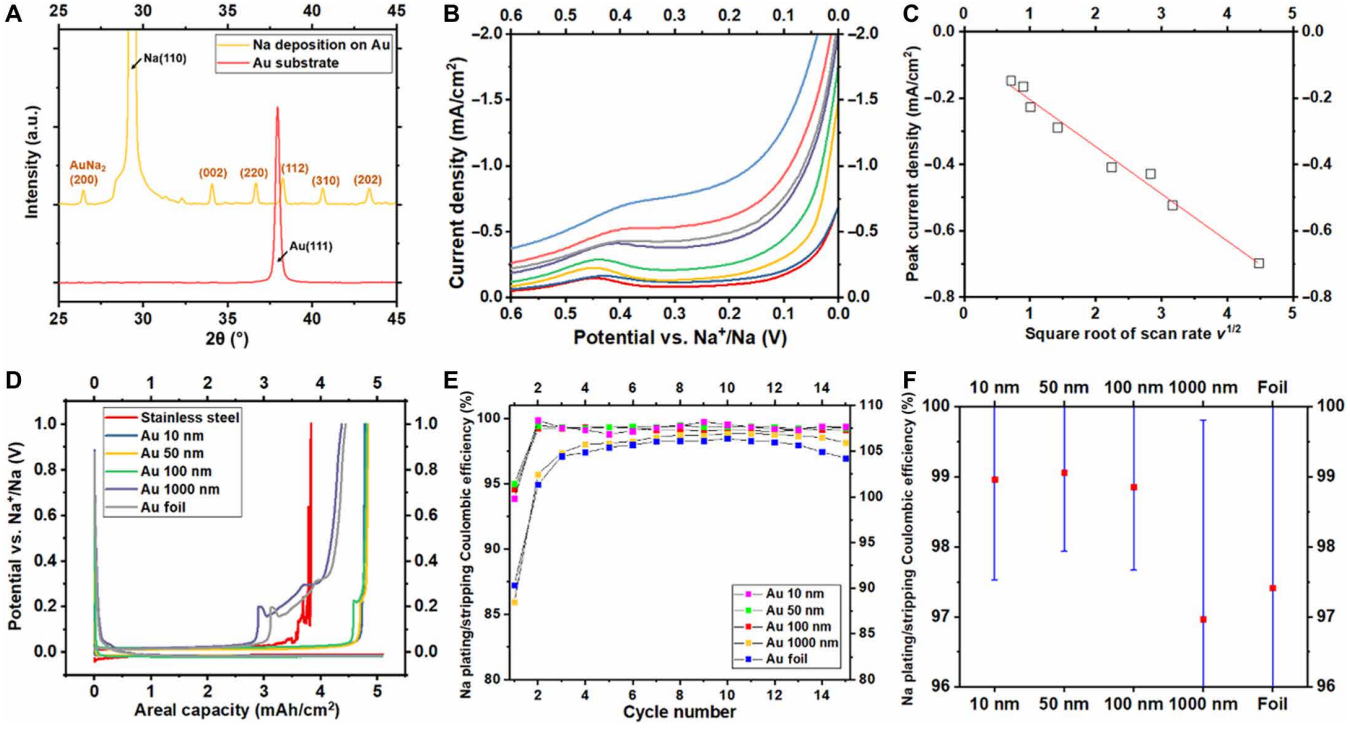

Fig. 7. Evaluation of the Sabatier-like principle for Na metal battery anodes. (**A**) XRD of the original Au substrate (red) and the Au substrate after Na electrodeposition (yellow). Substrate: 100-nm Au deposited on SS. a.u., arbitrary units. (**B**) CV scans of Na on Au foil at representative rates. (**C**) Plot of peak current density versus the square root of scan rate (i_p versus $v^{1/2}$, in $V^{1/2}/s^{1/2}$). (**D**) Galvanostatic plating/stripping voltage profiles for Na on Au substrates of different thicknesses (i.e., bare SS, 10-nm Au, 50-nm Au, 100-nm Au, 1000-nm Au, and thick foil-type Au). Galvanostatic plating/stripping CE values for Na on Au substrates with different thicknesses: (**E**) distribution over cycle number and (**F**) run-to-run averages and statistics.

designing advanced Li-sulfur cathodes by achieving optimal interaction between the polysulfides and the host materials guided by a similar Sabatier-type relation. Under these conditions, mechanical detachment of metal deposits (i.e., dead metal formation) and excessive bulk phase transition, which pulverizes the substrate, can both be prevented. A rule-of-thumb criterion is that the formation enthalpy of the intermetallic species formed should be slightly negative; very roughly, this optimal value is estimated to be around −0.02 to −0.04 eV per formula unit. The study also demonstrates that advanced surface characterization tools (e.g., FIB and aberration-corrected STEM) provide a robust approach for probing these critical electrochemical interfaces with high spatial and chemical resolution. The electroanalytical and structural characterization results together reveal the distinct natures of the chemical kinetics occurring at the heterointerfaces. We further show that this knowledge can be translated to guide the materials design of advanced battery anodes with much less need for excess metal in the anode but that exhibit stable, long-term cycling behaviors.

MATERIALS AND METHODS

Materials

Zn foil (99.9%), $ZnSO_4{\cdot}7H_2O$ (99.95%), V_2O_5 (99.95%), NaCl (99%), sodium hexafluorophosphate ($NaPF_6$), and glycol dimethyl were purchased from Sigma-Aldrich. Ta foil (99.95%; 0.025 mm), Au foil (99.95%; 0.025 mm), Ag foil (99.95%; 0.025 mm), and 304 SS foil (0.025 mm) were bought from Alfa Aesar. Cu foil (99.8%; 0.025 mm) and Al foil (99.3%; 0.015 mm) were purchased from MTI. The foils were used as received unless otherwise specified. Deionized water was obtained from Milli-Q water purification system. The resistivity of the deionized water is 18.2 megohm·cm at room temperature. Zn electrolytes were prepared by dissolving $ZnSO_4{\cdot}7H_2O$ into the deionized water (2 M). Cu electrolytes were prepared by dissolving $CuSO_4{\cdot}5H_2O$ into the deionized water (1 M). Electrolyte for Na cells was prepared in the laboratory by dissolving 1.0 M $NaPF_6$ in anhydrous, 99.5% diethylene glycol dimethyl ether, followed by further drying using molecular sieve. Plain carbon cloth 1071 HCB was purchased from Fuel Cell Store. Ketjen Black (KB) carbon was purchased from AkzoNobel. SS 304 discs with a diameter of 15.8 mm were polished on-site using a VibroMet vibratory polisher, using Final-POL polishing cloth and 0.3-μm alumina slurry. Polished SS discs were coated with a thin layer of Au by magnetron argon sputtering deposition system.

Characterization of materials

Field-emission SEM was carried out on Zeiss Gemini 500 scanning electron microscope. CV was performed using a CH 600E electrochemical workstation. XRD was performed on a Bruker D8 general area detector diffraction system with a Cu or a Co Kα x-ray source and a Bruker D8 powder diffractometer. Galvanostatic measurements were carried out using Neware battery testing system. AFM was performed on Cypher ES (Asylum Research Inc.). FIB was performed on the VELION system manufactured by Raith. A Zeiss Gemini scanning electron microscope system was used to obtain the secondary electron images and the energy-dispersive spectroscopy results. Aberration-corrected high-angle annular dark-field–STEM was carried out on FEI Themis Z G3. The materials characterization was performed, in part, at the MIT.nano Characterization Facility.

XPS data were collected at the Center for Functional Nanomaterials at Brookhaven National Laboratory, NY, in an ultrahigh vacuum chamber equipped with a SPECS Phoibos 100 MCD analyzer and nonmonochromatized Al Kα (hν = 1486.6 eV) x-ray source. The experiments were carried out using an accelerating voltage of 12 kV and a current of 20 mA, with a base chamber pressure of 2×10^{-9} torr. Cycling was terminated with a deposition step to a capacity of 0.1 mAh/cm^2. For all cycled samples, data were collected in the as-prepared state and after 45 min of Ar sputtering, performed at room temperature with a pressure of 2×10^{-5} torr with an energy of 1.5 keV. Electrodes were pressed onto a conductive Cu tape and mounted on the sample holder. Charge correction was performed by calibrating the Zn 2p binding energy to 1022 eV for Zn $2p_{3/2}$ spectra for cycled samples and 284.8 eV for adventitious carbon for pristine foils. Data were analyzed using CasaXPS software. A Shirley background was subtracted before peak deconvolution. Fitting was performed using a mixed Lorentzian-Gaussian line shape.

The operando isothermal microcalorimetry (IMC) measurements were performed with a TA Instruments TAM IV microcalorimeter. Coin-type cells were placed in IMC ampules submerged in an oil bath where the temperature was rigorously maintained at 30°C. All operando electrochemistry tests were controlled using a BioLogic VSP potentiostat. The cells monitored by the IMC were charged or discharged at a constant current of 0.8 mA/cm^2 for 5 cycles. A voltage limit of 1.0 V (versus Zn/Zn^{2+}) was used for metal stripping (charge, oxidation), while an areal capacity limit of 0.8 mAh/cm^2 was used to control the metal plating (discharge, reduction). Between each plating/stripping step, a 1-hour open-circuit rest was introduced to ensure thermal equilibration.

Electrochemical measurements

Fabrication of the cathode

$NaV_3O_8{\cdot}1.5H_2O$ (NVO) was synthesized according to a prior study (*53*). One gram of V_2O_5 powder was mixed with 15 ml of 2 M NaCl solution. The mixture was stirred for 96 hours at room temperature. The product was washed and collected after freeze drying. The NVO material was mixed with KB and polyvinylidene fluoride (weight ratio of 80:10:10) and dispersed into carbon cloth following a procedure reported in our previous study (*52*).

Coin cell fabrication

CR2032 coin cells were used. Electrodes are separated by glass fiber (Whatman) filter membranes. The thickness of a piece of free-standing glass fiber separator before battery assembling is on the order of hundreds of micrometers (200 to 400 μm). The effective thickness of the membranes is reduced under pressure when used in coin cells. In each cell, ~100 μl of electrolyte was added by pipette.

Cu deposition on SS

The electrodeposition of Cu on SS was performed at a constant potential at −0.5 V versus Cu^{2+}/Cu in coin cells. A piece of Cu foil was used as the reference/counter electrode; SS was used as the substrate (working electrode). The areal capacity of the deposited Cu is 0.3 mAh/cm^2, corresponding to a ~400-nm theoretical thickness.

CE measurement

See fig. S2 for details. The metal plating/stripping CE = $\frac{\text{stripping capacity}}{\text{plating capacity on the substrate}} \times 100\%$, which quantifies the reversibility of the metal anode. For example, CE = 100% means that all the plated Zn on the substrate can be stripped, while CE = 80% means that 80% of plated Zn can be stripped and 20% Zn is electrochemically inactive.

SUPPLEMENTARY MATERIALS

Supplementary material for this article is available at https://science.org/doi/10.1126/sciadv.abq6321

REFERENCES AND NOTES

1. J. W. Erisman, M. A. Sutton, J. Galloway, Z. Klimont, W. Winiwarter, How a century of ammonia synthesis changed the world. *Nat. Geosci.* **1**, 636–639 (2008).
2. M. J. Sterba, V. Haensel, Catalytic reforming. *Ind. Eng. Chem. Prod. Res. Dev.* **15**, 2–17 (1976).
3. D. S. Newsome, The water-gas shift reaction. *Catal. Rev. Sci. Eng.* **21**, 275–318 (1980).
4. G. C. Bond, *Heterogeneous Catalysis* (Oxford Univ. Press, 1987).
5. E. Roduner, Understanding catalysis. *Chem. Soc. Rev.* **43**, 8226–8239 (2014).
6. A. A. Baladin, Modern state of the multiplet theory of heterogeneous catalysis. *Adv. Catal.* **19**, 1–20 (1969).
7. J. K. Nørskov, T. Bligaard, A. Logadottir, S. Bahn, L. B. Hansen, M. Bollinger, H. Bengaard, B. Hammer, Z. Sljivancanin, M. Mavrikakis, Y. Xu, S. Dahl, C. J. H. Jacobsen, Universality in heterogeneous catalysis. *J. Catal.* **209**, 275–278 (2002).
8. G. Jerkiewicz, Standard and reversible hydrogen electrodes: Theory, design, operation, and applications. *ACS Catal.* **10**, 8409–8417 (2020).
9. Y. Liang, H. Dong, D. Aurbach, Y. Yao, Current status and future directions of multivalent metal-ion batteries. *Nat. Energy* **5**, 646–656 (2020).
10. L. Ma, M. A. Schroeder, O. Borodin, T. P. Pollard, M. S. Ding, C. Wang, K. Xu, Realizing high zinc reversibility in rechargeable batteries. *Nat. Energy* **5**, 743–749 (2020).
11. J. F. Parker, C. N. Chervin, I. R. Pala, M. Machler, M. F. Burz, J. W. Long, D. R. Rolison, Rechargeable nickel–3D zinc batteries: An energy-dense, safer alternative to lithium-ion. *Science* **356**, 415–418 (2017).
12. J. Zheng, Q. Zhao, T. Tang, J. Yin, C. D. Quilty, G. D. Renderos, X. Liu, Y. Deng, L. Wang, D. C. Bock, C. Jaye, D. Zhang, E. S. Takeuchi, K. J. Takeuchi, A. C. Marschilok, L. A. Archer, Reversible epitaxial electrodeposition of metals in battery anodes. *Science* **366**, 645 (2019).
13. S. Ichikawa, Volcano-shaped curves in heterogeneous catalysis. *Chem. Eng. Sci.* **45**, 529–535 (1990).
14. S. Higashi, S. W. Lee, J. S. Lee, K. Takechi, Y. Cui, Avoiding short circuits from zinc metal dendrites in anode by backside-plating configuration. *Nat. Commun.* **7**, 11801 (2016).
15. J. Zheng, L. A. Archer, Crystallographically textured electrodes for rechargeable batteries: Symmetry, fabrication, and characterization. *Chem. Rev.* **122**, 14440–14470 (2022).
16. J. Zheng, L. A. Archer, Controlling electrochemical growth of metallic zinc electrodes: Toward affordable rechargeable energy storage systems. *Sci. Adv.* **7**, eabe0219 (2021).
17. J. Zheng, Y. Deng, J. Yin, T. Tang, R. Garcia-Mendez, Q. Zhao, L. A. Archer, Textured electrodes: Manipulating built-in crystallographic heterogeneity of metal electrodes via severe plastic deformation. *Adv. Mater.* **34**, 2106867 (2022).
18. F. Wang, O. Borodin, T. Gao, X. Fan, W. Sun, F. Han, A. Faraone, J. A. Dura, K. Xu, C. Wang, Highly reversible zinc metal anode for aqueous batteries. *Nat. Mater.* **17**, 543–549 (2018).
19. X. Q. Zhang, X. B. Cheng, X. Chen, C. Yan, Q. Zhang, Fluoroethylene carbonate additives to render uniform Li deposits in lithium metal batteries. *Adv. Funct. Mater.* **27**, 1605989 (2017).
20. W. Dong, J. L. Shi, T. S. Wang, Y. X. Yin, C. R. Wang, Y. G. Guo, 3D zinc@carbon fiber composite framework anode for aqueous Zn–MnO_2 batteries. *RSC Adv.* **8**, 19157–19163 (2018).
21. C. Yang, Y. Yao, S. He, H. Xie, E. Hitz, L. Hu, Ultrafine silver nanoparticles for seeded lithium deposition toward stable lithium metal anode. *Adv. Mater.* **29**, 1702714 (2017).
22. X. Chen, X.-R. Chen, T.-Z. Hou, B.-Q. Li, X.-B. Cheng, R. Zhang, Q. Zhang, Lithiophilicity chemistry of heteroatom-doped carbon to guide uniform lithium nucleation in lithium metal anodes. *Sci. Adv.* **5**, eaau7728 (2019).
23. T. Foroozan, V. Yurkiv, S. Sharifi-Asl, R. Rojaee, F. Mashayek, R. Shahbazian-Yassar, Non-dendritic zn electrodeposition enabled by zincophilic graphene substrates. *ACS Appl. Mater. Interfaces* **11**, 44077–44089 (2019).
24. Y. Gu, H. Y. Xu, X. G. Zhang, W. W. Wang, J. W. He, S. Tang, J. W. Yan, D. Y. Wu, M. S. Zheng, Q. F. Dong, B. W. Mao, Lithiophilic faceted Cu (100) surfaces: High utilization of host surface and cavities for lithium metal anodes. *Angew. Chem. Int. Ed.* **58**, 3092–3096 (2019).
25. S. Xu, D. McOwen, C. Wang, L. Zhang, W. Luo, C. Chen, Y. Li, Y. Gong, J. Dai, Y. Kuang, C. Yang, T. R. Hamann, E. D. Wachsman, L. Hu, Three-dimensional, solid-state mixed electron-ion conductive framework for lithium metal anode. *Nano Letters* **18**, 3926–3933 (2018).
26. M. G. Chu, J. McBreen, G. Adzic, Substrate effects on zinc deposition from zincate solutions: I. Deposition on Cu, Au, Cd and Zn. *J. Eloectrochem. Soc.* **128**, 2281 (1981).
27. J. McBreen, M. G. Chu, G. Adzic, Substrate effects on zinc deposition from zincate solutions: II. Deposition on Pb, Tl, Sn, and In. *J. Eloectrochem. Soc.* **128**, 2287 (1981).
28. R. G. Compton, C. E. Banks, *Understanding Voltammetry* (World Scientific, 2018).
29. J. Horkans, I. C. H. Chang, P. C. Andricacos, H. Deligianni, Alloying of a less noble metal in electrodeposited Cu through underpotential deposition. *J. Electrochem. Soc.* **142**, 2244–2249 (1995).
30. M. Paunovic, M. Schlesinger, *Fundamentals of Electrochemical Deposition* (Wiley, 1998).
31. M. Forghani, S. W. Donne, Method comparison for deconvoluting capacitive and pseudo-capacitive contributions to electrochemical capacitor electrode behavior. *J. Electrochem. Soc.* **165**, A664–A673 (2018).
32. J. Zheng, J. Yin, D. Zhang, G. Li, D. C. Bock, T. Tang, Q. Zhao, X. Liu, A. Warren, Y. Deng, S. Jin, A. C. Marschilok, E. S. Takeuchi, K. J. Takeuchi, C. D. Rahn, L. A. Archer, Spontaneous and field-induced crystallographic reorientation of metal electrodeposits at battery anodes. *Sci. Adv.* **6**, eabb1122 (2020).
33. C. Fang, J. Li, M. Zhang, Y. Zhang, F. Yang, J. Z. Lee, M. H. Lee, J. Alvarado, M. A. Schroeder, Y. Yang, B. Lu, N. Williams, M. Ceja, L. Yang, M. Cai, J. Gu, K. Xu, X. Wang, Y. S. Meng, Quantifying inactive lithium in lithium metal batteries. *Nature* **572**, 511–515 (2019).
34. J. Zheng, R. Garcia-Mendez, L. A. Archer, Engineering multiscale coupled electron/ion transport in battery electrodes. *ACS Nano* **15**, 19014–19025 (2021).
35. J. Zheng, T. Tang, Q. Zhao, X. Liu, Y. Deng, L. A. Archer, Physical orphaning versus chemical instability: Is dendritic electrodeposition of Li fatal? *ACS Energy Lett.* **4**, 1349–1355 (2019).
36. W. A. Owczarski, Diffusion welding. *SAE Trans.*, 537–548 (1965).
37. M. Schlesinger, M. Paunovic, *Modern Electroplating* (John Wiley & Sons, 2011), vol. 55.
38. K. Edalati, Z. Horita, Significance of homologous temperature in softening behavior and grain size of pure metals processed by high-pressure torsion. *Mater. Sci. Eng. A* **528**, 7514–7523 (2011).
39. M. N. Obrovac, V. L. Chevrier, Alloy negative electrodes for Li-ion batteries. *Chem. Rev.* **114**, 11444–11502 (2014).
40. G. Taillades, J. Sarradin, Silver: High performance anode for thin film lithium ion batteries. *J. Power Sources* **125**, 199–205 (2004).
41. R. A. Huggins, Lithium alloy negative electrodes. *J. Power Sources* **81-82**, 13–19 (1999).
42. S. G. Fries, T. Jantzen, Compilation of `CALPHAD' formation enthalpy data: Binary intermetallic compounds in the COST 507 Gibbsian database. *Thermochim. Acta* **314**, 23–33 (1998).
43. A. Jain, S. P. Ong, G. Hautier, W. Chen, W. D. Richards, S. Dacek, S. Cholia, D. Gunter, D. Skinner, G. Ceder, K. A. Persson, Commentary: The Materials Project: A materials genome approach to accelerating materials innovation. *Apl Mater.* **1**, 011002 (2013).
44. W. Li, L. M. Housel, G. P. Wheeler, D. C. Bock, K. J. Takeuchi, E. S. Takeuchi, A. C. Marschilok, Thermodynamic analysis of LiNi0.6Mn0.2Co0.2O2 (NMC622) voltage hysteresis induced through high voltage charge. *ACS Appl. Energy Mater.* **4**, 12067–12073 (2021).
45. K. Hoshino, Y. Iijima, K.-I. Hirano, Intrinsic diffusion coefficients and the vacancy flow factor in dilute Cu-Zn Alloys. *Metall. Trans. A.* **13**, 1135–1139 (1982).
46. G. H. Cheng, M. A. Dayananda, R. E. Grace, Diffusion studies in Ag-Zn alloys. *Metall. Trans. A.* **6**, 21–27 (1975).
47. A. L. Hurley, M. A. Dayananda, Multiphase diffusion in Ag-Zn alloys. *Metallurg. Trans.* **1**, 139–143 (1970).
48. C. K. Chan, H. Peng, G. Liu, K. McIlwrath, X. F. Zhang, R. A. Huggins, Y. Cui, High-performance lithium battery anodes using silicon nanowires. *Nat. Nanotechnol.* **3**, 31–35 (2008).
49. H. L. Hong, Q. Wang, C. Dong, P. K. Liaw, Understanding the Cu-Zn brass alloys using a short-range-order cluster model: Significance of specific compositions of industrial alloys. *Sci. Rep.* **4**, 7065 (2014).
50. K.-S. Zuo, S.-Q. Xi, J.-E. Zhou, Effect of temperature on mechanical alloying of Cu-Zn and Cu-Cr system. *Trans. Nonferrous Met. Soc. Chin.* **19**, 1206–1214 (2009).
51. J. Zheng, M. S. Kim, Z. Tu, S. Choudhury, T. Tang, L. A. Archer, Regulating electrodeposition morphology of lithium: Towards commercially relevant secondary Li metal batteries. *Chem. Soc. Rev.* **49**, 2701–2750 (2020).
52. J. Zheng, Q. Zhao, X. Liu, T. Tang, D. C. Bock, A. M. Bruck, K. R. Tallman, L. M. Housel, A. M. Kiss, A. C. Marschilok, E. S. Takeuchi, K. J. Takeuchi, L. A. Archer, Nonplanar electrode architectures for ultrahigh areal capacity batteries. *ACS Energy Lett.* **4**, 271–275 (2019).
53. F. Wan, L. Zhang, X. Dai, X. Wang, Z. Niu, J. Chen, Aqueous rechargeable zinc/sodium vanadate batteries with enhanced performance from simultaneous insertion of dual carriers. *Nat. Commun.* **9**, 1656 (2018).
54. C. Zhu, R. E. Usiskin, Y. Yu, J. Maier, The nanoscale circuitry of battery electrodes. *Science* **358**, eaao2808 (2017).
55. J. Cui, X. Liu, Y. Xie, K. Wu, Y. Wang, Y. Liu, J. Zhang, J. Yi, Y. Xia, Improved electrochemical reversibility of Zn plating/stripping: A promising approach to suppress water-induced issues through the formation of H-bonding. *Mater. Today Energy* **18**, 100563 (2020).
56. F. Cocco, B. Elsener, M. Fantauzzi, D. Atzei, A. Rossi, Nanosized surface films on brass alloys by XPS and XAES. *RSC Adv.* **6**, 31277–31289 (2016).
57. B. R. Strohmeier, Copper/silver/gold alloy by XPS. *Surf. Sci. Spectra* **3**, 175–181 (1994).
58. R. G. Jordan, D. M. Zehner, N. M. Harrison, P. J. Durham, W. M. Temmerman, An XPS investigation of the electronic structure in AgZn. *Zeitschrift für Physik B Condensed Matter* **75**, 291–295 (1989).

59. T. Darrah Thomas, P. Weightman, Valence electronic structure of AuZn and AuMg alloys derived from a new way of analyzing Auger-parameter shifts. *Phys. Rev. B* **33**, 5406–5413 (1986).
60. F. Kiani, N. A. Astani, R. Rahighi, A. Tayyebi, M. Tayebi, J. Khezri, E. Hashemi, U. Rothlisberger, A. Simchi, Effect of graphene oxide nanosheets on visible light-assisted antibacterial activity of vertically-aligned copper oxide nanowire arrays. *J. Colloid Interface Sci.* **521**, 119–131 (2018).
61. P. Quaino, F. Juarez, E. Santos, W. Schmickler, Volcano plots in hydrogen electrocatalysis–uses and abuses. *Beilstein J. Nanotechnol.* **5**, 846–854 (2014).
62. H. Kim, M. Seo, M. H. Park, J. Cho, A critical size of silicon nano-anodes for lithium rechargeable batteries. *Angew. Chem. Int. Ed.* **49**, 2146–2149 (2010).
63. Y. Deng, J. Zheng, A. Warren, J. Yin, S. Choudhury, P. Biswal, D. Zhang, L. A. Archer, On the reversibility and fragility of sodium metal electrodes. *Adv. Energy Mater.* **9**, 1901651 (2019).
64. Y. Deng, J. Zheng, Q. Zhao, J. Yin, P. Biswal, Y. Hibi, S. Jin, L. A. Archer, Highly reversible sodium metal battery anodes via alloying heterointerfaces. *Small* **18**, 2203409 (2022).
65. J. Zheng, D. C. Bock, T. Tang, Q. Zhao, J. Yin, K. R. Tallman, G. Wheeler, X. Liu, Y. Deng, S. Jin, A. C. Marschilok, E. S. Takeuchi, K. J. Takeuchi, L. A. Archer, Regulating electrodeposition morphology in high-capacity aluminium and zinc battery anodes using interfacial metal–substrate bonding. *Nat. Energy* **6**, 398–406 (2021).

Acknowledgments: We express our gratitude to M. Pfeifer, X. Ren, and R. Luo for valuable discussions. **Funding:** This work was supported as part of the Center for Mesoscale Transport Properties, an Energy Frontier Research Center supported by the U.S. Department of Energy, Office of Science, Basic Energy Sciences, under award #DE-SC0012673. This work made use of the Cornell Center for Materials Research Shared Facilities, which are supported through the NSF MRSEC program (DMR-1719875). This work made use of the MIT.nano Characterization Facilities (Gemini SEM, Raith VELION FIB-SEM, Themis Z G3). **Author contributions:** L.A.A. directed the project. J.Z. and L.A.A. conceived and designed this work. J.Z., Y.D., J.Y., and T.T. performed the electrodeposition, electrochemical measurements, and structure characterizations. W.L., P.J.W., X.T., D.C.B., K.J.T., E.S.T., and A.C.M. performed the XPS and IMC experiments. All the authors analyzed and discussed the data. J.Z., L.A.A., and Y.D. wrote the manuscript with important inputs from all the authors. **Competing interests:** The authors declare that they have no competing interests. **Data and materials availability:** All data needed to evaluate the conclusions in the paper are present in the paper and/or the Supplementary Materials.

Submitted 20 April 2022
Accepted 16 September 2022
Published 4 November 2022
10.1126/sciadv.abq6321